Advanced Intensity-Modulation Continuous-Wave Lidar Techniques for ASCENDS CO2 Column Measurements

Joel F. Campbell, Bing Lin, Amin R. Nehrir, F. Wallace Harrison, Michael D. Obland, Byron Meadows

NASA Langley Research Center, Hampton, VA 23681
joel.f.campbell@nasa.gov

Global atmospheric carbon dioxide (CO2) measurements for the NASA Active Sensing of CO2 Emissions over Nights, Days, and Seasons (ASCENDS) space mission are critical for improving our understanding of global CO_2 sources and sinks. Advanced Intensity- Modulated Continuous-Wave (IM-CW) lidar techniques are investigated as a means of facilitating CO2 measurements from space to meet the ASCENDS measurement requirements. In recent numerical, laboratory and flight experiments we have successfully used the Binary Phase Shift Keying (BPSK) modulation technique to uniquely discriminate surface lidar returns from intermediate aerosol and cloud contamination. We demonstrate the utility of BPSK to eliminate sidelobes in the range profile as a means of making Integrated Path Differential Absorption (IPDA) column CO2 measurements in the presence of optically thin clouds, thereby eliminating the need to correct for sidelobe bias errors caused by the clouds. Furthermore, high accuracy and precision ranging to the surface as well as to the top of intermediate cloud layers, which is a requirement for the inversion of column CO_2 number density measurements to column CO2 mixing ratios, has been demonstrated using new hyperfine interpolation techniques that takes advantage of the periodicity of the modulation waveforms. This approach works well for both BPSK and linear swept-frequency modulation techniques. The BPSK technique under investigation has excellent auto-correlation properties while possessing a finite bandwidth. A comparison of BPSK and linear swept-frequency is also discussed in this paper. These results are extended to include Richardson-Lucy deconvolution techniques to extend the resolution of the lidar beyond that implied by limit of the bandwidth of the modulation, where it is shown useful for making tree canopy measurements.

1. Introduction

The ability of lidar to penetrate to the ground through gaps in tree canopies makes it especially attractive for generating bare earth terrain models in forested areas. In addition, lidar can tell us much about the vegetation itself. Depending on the sensor type and collection parameters, a lidar system can either record multiple returns from a single transmitted pulse from the top of the tree canopy, intermediate layers of the canopy, as well from the ground, or can record all of the laser energy returned in a continuous waveform.

Attempts to use lidar to map forests with profiling laser altimeters first appeared in literature in 1980s [1,2] and in the 1990s, a number of efforts validated the use of lidar for forestry inventories [3,4,5]. Currently, many forestry firms and government agencies throughout the world use lidar technology for mapping, inventory, and resource management [6, 7, 8].

For trees, canopy height is the most common forest characteristic that is of importance. Since so much is known about the biophysical attributes of individual tree species, height is the driver in estimating wood volume, evaluation of local vegetation productivity, estimating biomass, predicting potential yield, commercial value, and fire behavior. Lidar has proven to be very successful in estimating tree heights. The measurement of tree height for an individual tree is defined as the vertical distance from the base of the tree to the topmost terminal bud. The measurement of tree height is estimated from lidar by subtracting the highest elevation return from the lowest elevation return closest to the tree.

For clouds it is extremely important to measure cloud height and thickness especially for low level clouds which are a key for cloud climate feedbacks [9, 10]. Measurements of the height and thickness of these low level clouds would provide direct information on the surface level moisture and boundary layer turbulence since the marine boundary layer clouds are generally produced by adiabatic lifting processes of surface moisture. The base and top of the clouds represent the lifting condensation level and buoyancy potential of surface moist air [11, 12]. For high clouds deep convection activities and rainfall efficiency, driving factors for high cloud feedbacks, are related to the cloud heights [13]. Advanced knowledge of physical properties of boundary layer and high clouds will significantly improve model predictions of cloud feedbacks and future climates.

One problem is that the measurements typically require a vertical-sampling resolution of 0.15-0.3 m and a pulse width of 3-10 meters to obtain useful information about trees. For clouds, thin cirrus clouds can be as thin as 60 m and boundary layer clouds can be of the order of 200-300 m. This limits lidar's usage in forest and some cloud applications. With signal processing, some other lower resolution lidars that were designed for a different purpose may be used. In a recent study the Richardson-Lucy algorithm, which is normally used to enhance astronomical images [14], was proposed to improve the resolution of a high-resolution lidar for the measurement of tree canopies [15]. However, this lidar had a sampling resolution of 0.15 m and a pulse width of 2-16 m and the improvement was only moderate. For our preliminary focus, we have been working to develop a lidar system to measure atmospheric CO_2 for the ASCENDS space mission [16, 17, 18]. As we have shown in recent flight tests, the vertical-sampling resolution of even a low-resolution lidar with a digitized-sampling resolution of 75 m can be enhanced to as high as 0.15 m under our processing conditions [19] and the synthetic pulse width can be improved from a measured 352 m to less than 5 m [20]. The spatial sample rate determines the ability to measure distances from a hard target and the pulse width determines the ability to resolve one object from another (canopy vs. ground for instance). Without further processing our ability to resolve different objects in the same frame would be limited to about 352 m in this case and our ability to measure range would be limited about ± 37.5 m. So our super-resolution technique is a major advancement for this application. What makes this possible is using a near exact interpolation we have developed [19] in combination with our new two-stage Richardson-Lucy algorithm [20]. This is a two-step approach: enhance vertical resolution first, and, then, deconvolve the signals from extended targets such as clouds and forest canopies to obtain super-resolution vertical profiles with resolution-enhanced data. Even though the starting vertical resolution is crude, the information is embedded in the phase of received signals so one can look at many low-resolution profiles of these signals simultaneously to reconstruct a high-resolution vertical profile. So far this has been demonstrated on a prototype intensity-modulated (IM) continuous wave (CW) lidar designed to measure atmospheric CO_2 concentration for the ASCENDS mission, but it could be reformulated for low resolution pulse systems such as the Cloud-Aerosol LIdar with Orthogonal Polarization (CALIOP) onboard CALIPSO satellite or some other lidar systems. Another possible application for the algorithm would be to build a low data rate lidar system capable of making atmospheric measurements, where the data rate is low enough to downlink the raw data in full and to process the data on the ground, making this a basis for a new compressive sensing system.

2 Super-resolution algorithm description

2.1 CW Measurement concept

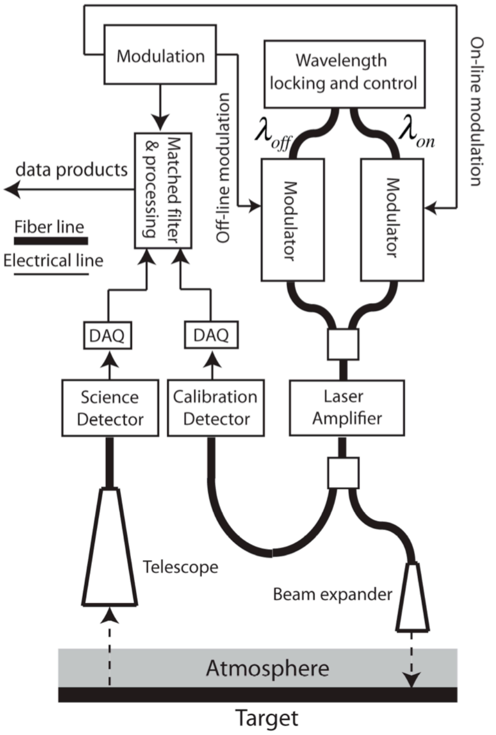

Fig. 1. Baseline instrument block diagram.

The concept of our IM-CW system designed for CO_2 integrated path differential absorption (IPDA) measurements is illustrated in Fig. 1. For the system described in this Fig. 1, intensity modulated online and offline seed lasers with distinct spectral properties are combined using fiber optics and simultaneously amplified using a single Erbium Doped Fiber Amplifier (EDFA) to increase the transmitted power. A small fraction of the transmitted beam is picked off via an optical tap inside of the EDFA and sent to a reference detector for power normalization. The backscattered science signals of the online and offline wavelengths from the surface as well as aerosols and clouds are simultaneously collected with a telescope, optically filtered with a narrow band optical filter, and detected by a single detector. Both the science and reference signals are amplified, electronically filtered and then digitized for retrievals of column CO_2 using IPDA approach. Post processing of the digitized science and reference data allows for discrimination between ground and intermediate scatterers using the matched filter technique. One also obtains differential absorption power ratios for inference of CO_2 column amounts as well as range estimates to the scattering targets. The on-line and off-line laser modulation signals can be expressed as

$$\Lambda_{off} = 1 + m\xi_{off}(t),\ \Lambda_{on} = 1 + m\xi_{on}(t), \tag{1}$$

where m is the modulation depth with a value between 0 and 1. The quantity $\xi(t)$ is the repeating modulation waveform where $-1 \le \xi(t) \le 1$ and $\langle \xi(t) \rangle = 0$. In general, the on- and off-line waveforms are chosen to be orthogonal to each other to avoid interference between channels.

Given the modulation waveforms presented in Eq.1, the instantaneous received lidar off-line and on-line powers ($P^R_{off}(t)$ and $P^R_{on}(t)$, respectively) from a single hard scatterer at range r are given by

$$
\begin{aligned}
P^R_{on,k}(t) &= \frac{K_k}{r^2}\,\overline{P^T_{on,k}}\exp\left(-2S\int_0^r \beta(r')dr'\right)\exp(-2\tau)\exp(-2\tau')\left(1+m\xi_{on}(t-2r/c)\right),\\
P^R_{off,k}(t) &= \frac{K_k}{r^2}\,\overline{P^T_{off,k}}\exp\left(-2S\int_0^r \beta(r')dr'\right)\exp(-2\tau)\left(1+m\xi_{off}(t-2r/c)\right),
\end{aligned}
\tag{2}
$$

where τ is the total one-way column optical depth for the off-line measurement that is determined by the gas absorption from molecules other than CO_2, and τ' is the one-way column optical depth resulting from CO_2 absorption only, β is the backscatter coefficient ($km^{-1}sr^{-1}$), S is the extinction to backscatter ratio (sr^{-1}), K_k is a function of the kth scatterer's reflectivity, and $\overline{P^T_{off}}$ and $\overline{P^T_{on}}$ are the average transmitted off-line and on-line powers over one period of the modulation waveform, respectively.

When multiple targets including the surface exist in the lidar path length, each target would generate similar received lidar signals like those in Eq. 2. The signals from these multiple targets are combined at the detector and converted to an electronic signal *s*(*t*). For an AC coupled receiver subsystem, we have,

$$
s(t) = \sum_k \left[C_{1k} m\xi_{on}(t-2r_k/c) + C_{2k} m\xi_{off}(t-2r_k/c)\right]
\tag{3}
$$

where we sum over all k scatterers and where,

$$
\begin{aligned}
C_{1k} &= \frac{K_k'}{r^2}\,\overline{P^T_{on}}\exp\left(-2S\int_0^{r_k} \beta(r')dr'\right)\exp(-2\tau_k)\exp(-2\tau_k'),\\
C_{2k} &= \frac{K_k'}{r^2}\,\overline{P^T_{off}}\exp\left(-2S\int_0^{r_k} \beta(r')dr'\right)\exp(-2\tau_k),
\end{aligned}
\tag{4}
$$

where K' is a constant. These C_{1k} and C_{2k} returns can be uniquely discriminated from other returns from different scatterers using the matched filter with the transmitted waveform. These are also proportional to the average received optical power ($\overline{P^R_{off,\,k}}$ and $\overline{P^R_{on,\,k}}$) from the kth scatterer. For a ground target, solving for τ_g' gives

$$
\tau_g' = \frac{1}{2}\ln\left(\frac{C_{2g}\overline{P^T_{on}}}{C_{1g}\overline{P^T_{off}}}\right) \equiv \frac{1}{2}\ln\left(\frac{\overline{P^R_{off,\,g}}\;\overline{P^T_{on}}}{\overline{P^R_{on,\,g}}\;\overline{P^T_{off}}}\right),
\tag{5}
$$

where C_{1g} and C_{2g} are the ground returns. Once C_{1g} and C_{2g} are determined, the column optical depth for CO_2 can be found using Eq. 5. In general, this is done by cross correlating the reference waveform with the return signal *s*(*t*), i.e., by the matched filter technique as mentioned before.

2.2 Multi-swept Frequency modulation

The main advantage of the multi-sweep approach is one may achieve a high level of orthogonality between channels while using simultaneous channels that are very close in frequency. The advantage is that one may make simultaneous on-line/off-line measurements with virtually no crosstalk.

The modulation waveform for the kth orthogonal channel takes the form

$$\xi_k(t) = \cos(\phi_k(t)), \tag{6}$$

where

$$\phi_k(t) = 2\pi \int_0^t f_k(t')dt', \tag{7}$$

where f_k is the frequency for the k$_{\text{th}}$ channel defined by

$$f_k(t) = f_{0k} + f_{sweep}(t - T \ \text{int}(t/T)), \tag{8}$$

where T is the sweep period, f_{0k} is the start frequency, f_{sweep} is the sweep function, and $\text{int}(t/T)$ is the integer part of t/T. Let

$$\phi_{sweep}(t) = 2\pi \int_0^t f_{sweep}(t')dt'. \tag{9}$$

We now construct a continuous phase function for each channel such that

$$\phi_k(t) = 2\pi f_{0k} t + \phi_{sweep}(T)\text{int}(t/T) + \phi_{sweep}(t - T \ \text{int}(t/T)). \tag{10}$$

We digitize these waveforms at a sample rate f_s, a sample time of $\Delta t = 1/f_s$ and with a frame size of N points that includes M sweeps such that the total time for M sweeps is $MT \equiv N\Delta t$. We define a circular correlation such that

$$\begin{aligned} R(ref, data) &= \frac{1}{N}\sum_{m=0}^{N-1} ref^*(m)\ data(m+n) \\ &= DFT^{-1}\left(DFT^*(ref*)DFT(data)\right) \end{aligned}, \tag{11}$$

where ref is the reference waveform, data is the data collected either from the reference or science detector, and DFT is the digital Fourier transform. For our data processing, ref will take the form of $\exp(i\ \phi_j)$ because our correlation is performed in quadrature. The channel frequencies f_{0k} are chosen to make each channel orthogonal with every other channel such that

$$R\left(\exp(i\ \phi_j), \cos(\phi_k)\right) = 0,\ j \neq k \tag{12}$$

where $i=\sqrt{-1}$. Since each channel is orthogonal, the constants C_1 and C_2 will then be proportional to the peak of the cross correlation of the return signal with the reference kernel for channels 1 and 2 respectively and the range is determined by the delay in the correlation where distance is $r=c\ \delta t/2$ where c is the speed of light and δt is the time delay.

The general swept case is closely related to the unswept case [21] in that the choice of frequencies is similar if we use the average frequency over a single sweep. That is to say one may use average frequency of

$$\langle f_k \rangle = f_{0k} + \langle f_{sweep} \rangle = f_{0k} + \frac{1}{2\pi\tau}\phi_{sweep}(T) \tag{13}$$

with the results of the unswept case as a starting point to guess what the orthogonal start frequencies are. Though related, the swept case is somewhat more complicated in the choice of allowable start frequencies. The role of necessity in choosing start frequencies can be presented as

$$\begin{aligned} &f_{01} = \frac{n_1}{2MT} - \frac{\phi_{sweep}(T)}{2\pi T} > 0, \\ &f_{02} = f_{01} + \frac{n_2}{2MT}, \\ &\ldots, \\ &f_{0K} = f_{01} + \frac{n_K}{2MT}, \end{aligned} \tag{14}$$

where K is the number of channels and n_j is an integer. The autocorrelation function for each channel will have exactly M peaks. Generally speaking, if the number of channels is greater than 2, the number of sweeps must be greater than the number of channels (M>K). For the two-channel case we must have at least 2 sweeps. The integer n_1 is chosen to make the autocorrelation for the first channel have the same peak height for each sweep. Once this is done, n_j for the other channels are chosen to make each channel orthogonal with every other and the autocorrelation function for each channel has equal peak heights. In a four channel setup, for instance, this can usually be done quickly by evaluating the cross correlation between channels and autocorrelation functions.

For the linear sweep case we choose

$$f_{sweep}(t) = \Delta f \frac{t}{T},\ 0 \le t < T\ , \tag{15}$$

where Δf is the sweep bandwidth. This is a well-known case from radar and will result in a range resolution of

$$\delta r = \frac{c}{2\Delta f}, \tag{16}$$

where c is the speed of light. The unambiguous range is given by

$$r_{\max} = \frac{c\ T}{2}\,. \tag{17}$$

The frequency as a function of time for each channel is

$$f_j(t) = f_{0k} + \Delta f \frac{t - T\ \mathrm{int}(t/T)}{T}, \tag{18}$$

where $\mathrm{int}(t/T)$ is the integer part of t/T. The phase is

$$\phi k(t) = 2\pi\left[f_{0k}t + \frac{1}{2}\Delta f T\,\mathrm{int}(t/T) + \frac{\Delta f}{2T}\left(t - T\ \mathrm{int}(t/T)\right)^2 \right]. \tag{19}$$

In the continuum limit it can be shown the autocorrelation function shown in Fig. 2 is given by

$$\begin{aligned} \left|R\left(\exp(i\ \phi_k), \cos(\phi_k)\right)\right| &\approx \left| \begin{array}{l} \frac{1}{\tau}\int_0^{\tau-t} \exp\left(-i\ \phi_k(t')\right)\exp\left(i\ \phi_k(t'+t)\right)dt' + \\ \frac{1}{\tau}\int_{\tau-t}^{\tau} \exp\left(-i\ \phi_k(t')\right)\exp\left(i\ \phi_k(t'+t)\right)dt' \end{array} \right| \\ &= \left| \frac{\sin\left[\pi\ \Delta f\ t\left(1 - \frac{|t|}{T}\right)\right]}{2\pi\ \Delta f\ t\left(1 - \frac{|t|}{T}\right)} \right|, -T < t < T \end{aligned}\,. \tag{20}$$

In the above integration we ignore the lower sideband because that is mostly filtered out in the integration.

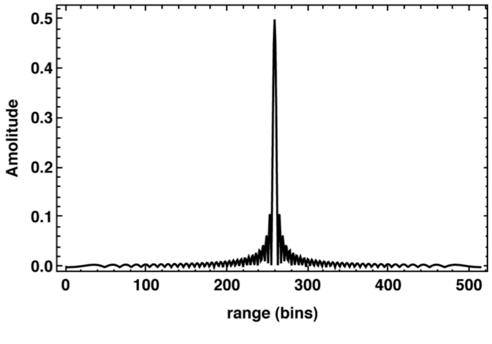

Fig. 2. Autocorrelation function using linear swept frequency modulation.

As an example we take the special case where we have a sample rate of 2000 kHz, a sweep bandwidth of 500 kHz, a frame size of 4096, and a sweep period of 512/2000 ms which results in M=8 sweeps per frame. We chose 4 channels and the parameters chosen that result in orthogonal sweeps are n_1=1450, n_2=18, n_3=30, and n_4=52. This results in start frequencies of approximately 104.004 kHz, 108.398 kHz, 111.328 kHz, and 116.699 kHz. Care must be taken to compute these as accurately as possible or choose parameters that result in start frequencies that are near integers to minimize round off error. Cross correlation crosstalk is 0 to within round off error in that case and between all other channels as well.

2.3 Binary Phase Shift Keying (BPSK)

The BPSK approach discussed here is where an IM sine wave carrier is modulated by a pseudo-noise (PN) code in the form of a maximum length (ML) sequence as in Eq. 21. To effectively represent each bit of ML-sequence in the transmitted waveforms, and allow flexibility in the unambiguous range for a particular code length and sample rate, we oversample the ML-sequence by an integer *M* such that each code bit of the ML sequence is represented by *M* points. Let $z_n \equiv z(n)$ be the original ML-sequence and $Z_n \equiv Z(n)$ be the oversampled ML-sequence such that $Z(n) = z(\mathrm{int}((n-1)/M)+1)$, where int(x) is a function that represents the integer part of x. The on and offline modulation waveform is given by,

$$\xi_k(t_n) = \xi_k(n/f_s) = (2Z(n)-1)\cos(2\pi n\, f_k/f_s), \tag{21}$$

where f_{on} is the online carrier frequency, f_{off} is the offline carrier frequency, and f_s is the sample rate. We could have more channels for different applications. A previous publication [21] describes a procedure for choosing orthogonal swept frequency signals where the starting frequency of the sweep is the desired parameter. We modify that slightly by choosing the center frequency as the desired parameter for a BPSK signal. Let us suppose we have exactly P repeats of the ML sequence in a frame of *N* points where the period of each repeat is *T*. We claim the center frequency of K orthogonal channels will take the form

$$f_{c1} = \frac{n_1}{2PT},\ f_{c2} = \frac{n_2}{2PT},\ \ldots,\ f_{ck} = \frac{n_k}{2PT}, \tag{22}$$

Not every choice of n_k will lead to orthogonal frequencies but the ones that are orthogonal will take that form. This form works best in situations where there are no multiple scatterers or where only ranging is needed as under clear skies. But a small flat background offset proportional to the inverse of the PN code length could exist. This does not present a problem unless there are multiple scatterers, where it could cause a small bias error in the peak height due to interference with other scatters. Choosing a very long PN code can minimize this effect. This reference waveform is given by

$$\Gamma_k(n) = (2Z(n)-1)\exp(2\pi i n f_{on}/f_s). \tag{23}$$

This improved form can be used to both clear and cloudy sky cases and has the advantage of a perfectly 0 background offset so there is no interference between scatters and no bias in the peak heights. In this case the reference signal is

$$\Gamma'_k(n) = Z(n)\exp(2\pi i n f_k/f_s). \tag{24}$$

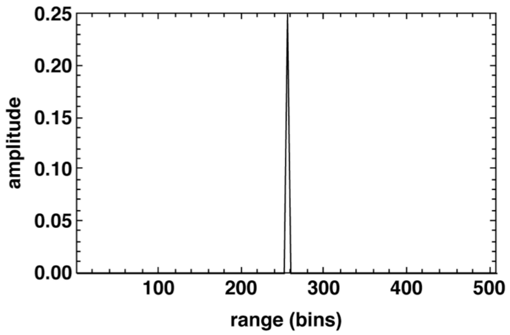

Fig. 3. Autocorrelation function using the BPSK modulation is completely lacking in sidelobes or other artifacts, which is the key advantage for using BPSK modulation.

An example of a 6-channel system that is mutually orthogonal using a frame size of 8128 (16, 127 point ML sequence repeats that were oversampled by a factor of 4) would be to choose center frequencies of {225125/508 kHz, 56875/127 kHz, 230125/508 kHz, 232625/508 kHz, 117625/254 kHz, 237625/508 kHz}. These are displayed as integer ratios so they may be computed in a more exact fashion to produce perfectly orthogonal BPSK waveforms. A plot of the autocorrelation function (derived from Eq. 11 and Eq. 24) is shown in Fig. 3, which is ideal in that it has no sidelobes or other artifact and is the synthetic pulse derived from the BPSK modulation.

Demodulation is accomplished simply by taking the magnitude of the matched filter correlation described by Eq. 11.

As an example of a modulation technique that is suitable for a band pass filtered LAS system presented in Fig. 1, we take the special case where P=16 (16 ML sequence repeats) and M=4 (4 samples per code bit) and choose a 2 MHz sample rate. We generate a 7th order (or 127 length) ML-sequence using the recurrence relation $z_{n+7} = z_n \oplus z_{n+6}$ with the seed {1, 0, 1, 0, 1, 1, 1}, where $\oplus$ is the “exclusive or”.

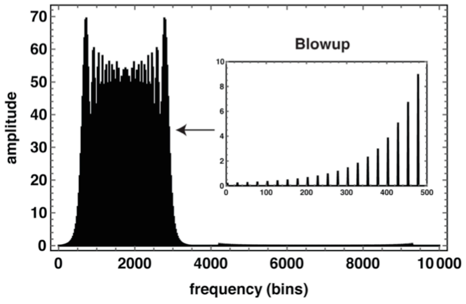

Fig. 4. Frequency spectrum of correlation before reordering shows spectrum is formed from a comb as we see from the blowup of the of the spectrum which shows a 25 point spacing between the teeth of the comb.

2.4 Fourier Transform Reordering (FTR) interpolation of periodic waveforms

Given that the DFT of the correlation forms a comb in the case of a repeating waveform and that the spacing between the teeth of the comb is equal to the number of repeats, we have shown that if one reorders the DFT array elements such that the spacing between the teeth is 0, one can effectively transform a periodic pulse train into a highly interpolated single pulse [19]. However, this must be done about a point equal to the center frequency of the spectrum plus the Nyquist rate such that all the teeth to the left of this point are moved to the left and all the teeth to the right of this point are moved to the right. This works because there is no mirror image in the frequency domain and it will therefore only have one unique spectrum since we are using the complex quadrature as the reference. The only requirement for this to work is that the signal must be sampled higher than the Nyquist rate. The reordered array is

$$\begin{aligned}
&f'(n) = f[n_0 + N_s(n-1)], \\
&\qquad 1 < n \le N_p/2 + N_c - 1, \\
&f'(n + N - N_p/2) = f[N_s(n - 1 + N_p/2) + n_0], \\
&\qquad N_c < n \le N_p/2, \\
&f'(n) = 0,\ \text{otherwise.}
\end{aligned} \tag{25}$$

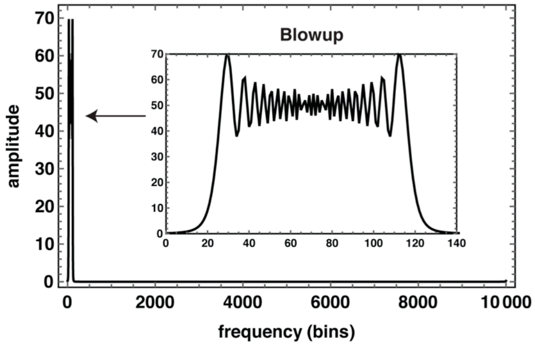

Fig. 5. Frequency spectrum after reordering with the comb tooth spacing reordered to 0 as is shown in the blowup.

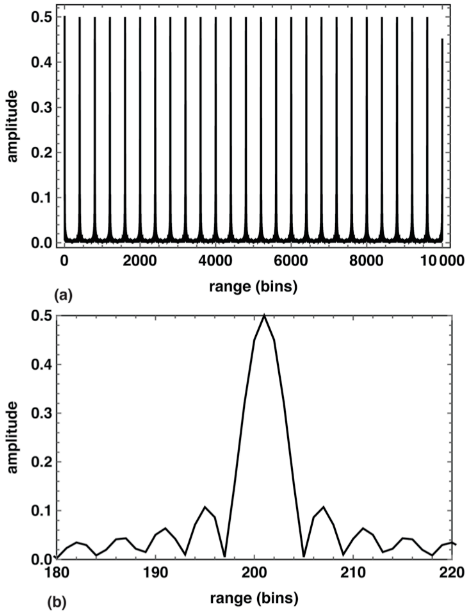

Fig. 6. Result of correlation before reordering shows periodic pulse profile with crude sampling.

Here *f'* is the new spectrum, *f* is the old spectrum, n_0 is the position of the first tooth of the comb, N_s is the number of sweeps/repeats, N is the total number of points, N_p is the number of points in one sweep/repeat, and N_c is the center frequency of the waveform in bins.

Alternatively we can do a cyclic rotation in the frequency domain such that the center frequency is mapped to 0. Then we can reorder the array such that all the teeth left of center are moved to the left and all teeth to the right of center are moved to the right. In this case one would use Eq. 25 with $N_c=0$. Both of the aforementioned methods work - the only difference is the phase term in the resulting correlation, which is removed when the magnitude is taken. The level of interpolation will be equal to the number of repeats in the DFT.

As an example we take a linear sweep case with 10000 points total with 25 sweeps. Fig. 4 shows a plot of the amplitude of the DFT of the correlation as described in Eq. 11 and shows how using the complex quadrature gives only one unique spectrum without a mirror image, thereby extending the Nyquist rate by a factor of 2. This is one of the many advantages to performing the correlation in quadrature. The blowup in Fig. 4 shows this spectrum is actually a comb. The tooth spacing in this case is 25 because we have 25 sweeps. Fig. 5 shows the spectrum after reordering with a comb tooth spacing of 0, which shows a more continuous curve.

Fig. 6a shows the resulting correlation before reordering. Since we are correlating multiple sweeps at once the result is multiple pulses. One can see from Fig. 6b the detail of each pulse shows crude sampling. Fig. 7a shows the resulting correlation after reordering results in a single pulse. The detail of this pulse shown in Fig. 7b exhibits fine sampling resulting from a factor of 25 improvement in the apparent sample rate.

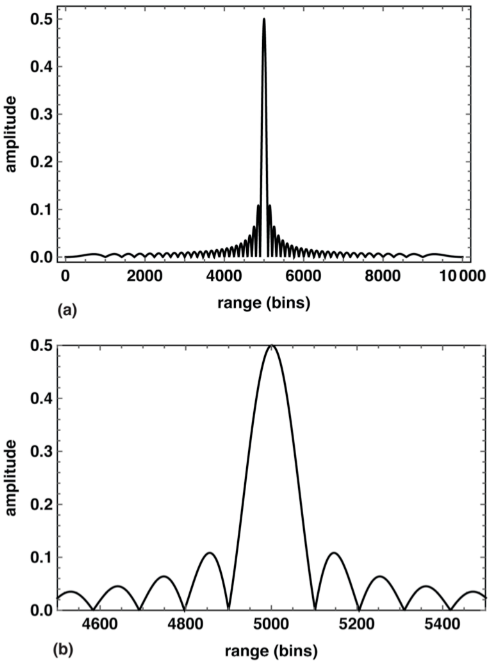

Fig. 7. Result of correlation after reordering shows crudely sampled periodic pulse train is converted into a single pulse that is oversampled by the number of repeats, which in this case is 25.

The theoretical explanation for this is the DFT of a function that is periodic within the range of the DFT forms a Kronecker comb. By changing the comb spacing to 0, the resulting inverse Fourier transform becomes non-periodic within the DFT range. Since the values outside of the comb are 0, this operation performs a type of Fourier interpolation. However, unlike normal Fourier interpolation we don't introduce extra points or 0s in the spectral domain – we just reorder the ones that already exist, which makes this technique very efficient. This technique [19] also saves tremendous computational time in order to increase ranging precision and accuracy compared to the time domain curve fitting and interpolation technique used previously [17][18].

2.5. Super-resolution by FTR interpolation and Richardson-Lucy (RL) deconvolution

After we take the magnitude of the resulting interpolated correlation obtained from Eqs. 11 and 25 we may further enhance this by implementing an accelerated RL algorithm [22] to deconvolute lidar returns from extended backscatteres for tree height and thickness estimations. The basic assumption used by RL is the measured image is given by

$$\lambda = \psi \otimes \rho + \eta \tag{26}$$

where λ is the measured image, ψ is the Point Spread Function (PSF), ρ is the undistorted image, η is the noise, and $\otimes$ is the convolution operator. The RL algorithm estimates the undistorted image iteratively by calculating N iterations of

$$\rho_{n+1} = \rho_n \left(\psi \,\hat{\otimes} \frac{\lambda}{\psi \otimes \rho_n} \right), \tag{27}$$

where ρ_n is the nth estimate of the undistorted image and $\hat{\otimes}$ is the correlation operator. Both the PSF and image are assumed to be positive with RL. Because we are using such a high degree of interpolation, we modify the algorithm further to second order by iterating with a new PSF derived from the original PSF such that we also calculate N iterations of

$$\psi'_{n+1} = \psi'_n \left(\psi \,\hat{\otimes} \frac{\psi}{\psi \otimes \psi'_n} \right), \tag{28}$$

where $\psi'_1 = \psi$. Then we refine the result further by calculating N' iterations of

$$\rho'_{n+1} = \rho'_n \left(\psi'_N \,\hat{\otimes} \frac{\rho_N}{\psi'_N \otimes \rho'_n} \right). \tag{29}$$

In this way it is possible to accelerate convergence by an order of magnitude or more beyond what is described by Biggs et. al. [22].

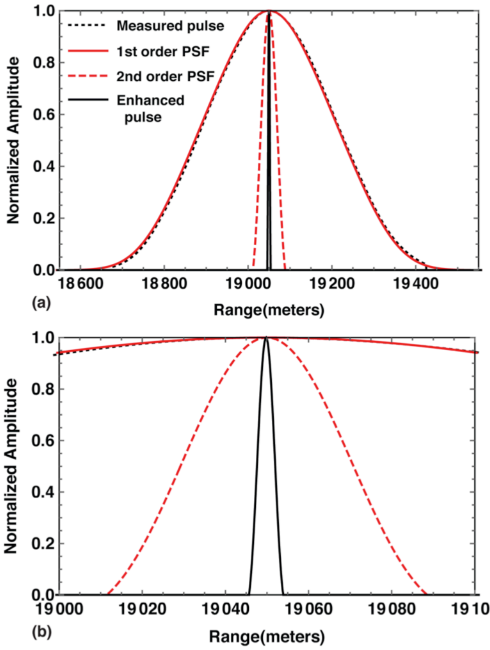

Fig. 8. Results of FTR interpolation and the two-stage RL deconvolution on the ground calibration measurement (a) and the zoomed in version (b). Using 100 first order iterations and 30 second order iterations the sample resolution goes from 75 m to .1875 m and the measured half height pulse width changes from 352 m to 4.40 m – almost 2 orders of magnitude. Data has been centered about 15 km.

This algorithm was recently tested during a series of airborne test flights for a newly developed IM-CW lidar system known as the ASCENDS CarbonHawk Experiment Simulator (ACES) [23]. The demonstration of these concepts was carried out where the instrument was operated at ~ 10 W avg. total power for three orthogonal transmitted channels and high altitude (~ 9-11.5 km). These three orthogonal waveforms were transmitted at three different wavelengths (1 on-line and 2 off-line wavelengths in the 1.571 µm CO_2 absorption band) where each transmitted wavelength had approximately 3.8 W, 3.5 W, and 2.7 W respectively of average power. Using the BPSK modulation described in section 2.2, the instrument operated at a sample rate of 2 MHz and a modulation code bitrate of 500 kbps, with 400 × 508 point repeats making a total frame length of 203200 [24], which gives us a sampling resolution of 75 meters and a theoretical pulse resolution of 300 m. Using FTR interpolation we transform a periodic 400-peak pulse train to a single pulse interpolated/sampled at 75/400 = 0.1875 m.

For the first test we did a ground experiment, where the laser was fed back to the receiver at close distance at low power. By taking the measured ground pulse and applying 100 1st order iterations using Eq. 27 and Eq. 28, then another 30 2nd order iterations using Eq. 29, we transform the pulse from a measured half height width of 352 m to 4.40 m, making the width resolution almost 2 orders of magnitude better as in Fig. 8.

The PSF was obtained by taking the theoretical ML-sequence, autocorrelation function, then filtering it with a periodic Gaussian filter [25]. Through a combination of instrument characterization and filtering to obtain the minimum pulse width from a hard ground return while still being able to see cloud and tree returns, we were able to obtain consistent results.

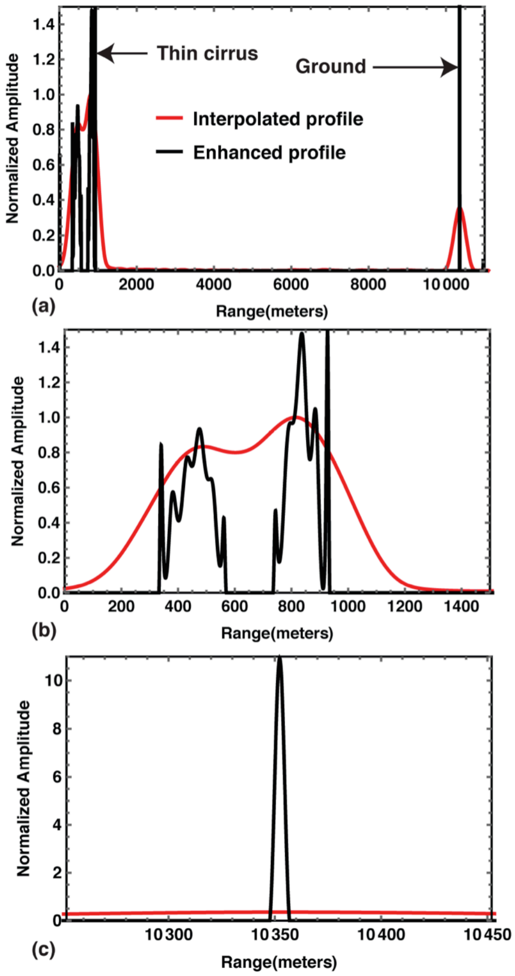

Fig. 9. Transmission through thin cirrus clouds (a) shows FTR interpolation combined with RL deconvolution is able to detect the thickness of thin cirrus clouds (b), yet the half height pulse width from the ground is also measured at about 4.91 m (c), which is only slightly wider than the 4.40 m enhanced pulse measured in ground testing.

We conducted many flight tests over ocean, land, and clouds. Fig. 9 shows a case where we transmitted through thin cirrus clouds and reflected from a hard surface. Despite the crude sampling resolution we are able to discern features well below the original 75 meter sampling and 352 m pulse width. One interesting feature is the change in relative pulse height. This can be explained by the algorithms tendency to preserve the area under the pulse. Since the ground pulse received from hard surface is compared to the thickness of the clouds, as one enhances the resolution the ground pulse becomes narrower and taller in comparison to the cloud pulse.

As a comparison we enhanced a ground return from forest trees, which is shown in

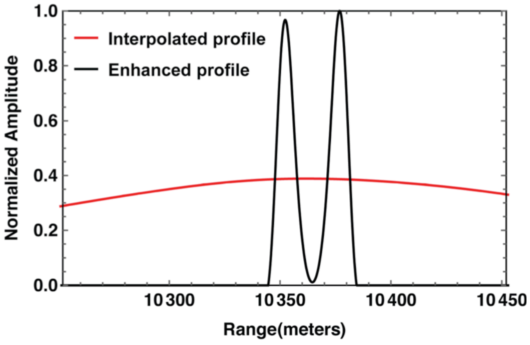

Fig. 10. RL enhanced pulse from tall trees shows tree height of about 30 m.

Fig. 10. Here we see an estimated tree height of about 30 m, which is consistent with the type of trees found in southern Virginia.

2.6 Extentions to pulse lidar

Thus far we have discussed CW lidar as has been implemented in the Langley ASCENDS effort. However, there is no reason this theory couldn't be modified to cover pulse lidar systems such as those used on CALIPSO and other programs, and since this type of lidars is more common there is a huge amount of data one could use to extract science from. Technically the difference is fairly simple to implement. Instead of using a reordered FFT of the correlation to do the interpolation, one would use a reordered FFT of a periodic pulse train multiplied by the appropriate comb filter. The Richardson-Lucy part of it would be identical. If awarded, we would extend this theory and our algorithm used in ASCENDS to include the most common pulse lidar systems and process available data such as CALIPSO data, Langley High Spectral Resolution Lidar (HSRL)[26] pulse data, etc.

3. Conclusion

These results show it is possible to increase both the sample rate and fundamental resolution from a CW ranging lidar where the signal is sampled greater than the Nyquist rate. Using the Fourier transform reordering interpolation technique to increase the sampling resolution and by iteratively applying the modified Richardson-Lucy technique presented here, it is possible to increase the resolution by almost two orders of magnitude in as has been demonstrated here. This makes it possible to measure tree canopy heights, and also opens the possibility of a compressive sensing lidar.

References

1. R. Nelson, W. Krabill, & G. MacLean, Determining forest canopy characteristics using airborne laser data. Remote Sensing of Environment, 15, 201-212 (1984).
2. R. Nelson, W. Krabill, & J. Tonelli, Estimating forest biomass and volume using airborne laser data. Remote sensing of environment, 24 , 247-267 (1988).
3. E. Naesset, Estimating timber volume of forest stands using airborne laser scanner data, Remote Sensing of Environment, 61, 246-253(1997).
4. M. A. Lefsky, W. B. Cohen, S. A. Acker, G. G. Parker, T. A. Spies, D. Harding, Lidar remote sensing of the canopy structure and biophysical properties of Douglas-fir western hemlock forests, Remote sensing of environment, 70, 339-361(1999).
5. J. B. Blair, D. L. Rabine, M. A. Hofton, The Laser Vegetation Imaging Sensor: a medium-altitude, digitisation-only, airborne laser altimeter for mapping vegetation and topography, ISPRS Journal of Photogrammetry and Remote Sensing, *54*, 115-122(1999).
6. M. A. Wulder and Seemann, D. Forest inventory height update through the integration of LIDAR data with segmented landsat imagery. Can. J. Remote Sens, 29, 536–543(2003)

7. E. Næsset, T. Gobakken, J. Holmgren, H. Hyyppä, J. Hyyppä, M. Maltamo, U. Söderman, Laser scanning of forest resources: the Nordic experience, Scandinavian Journal of Forest Research, 19, 482-499(2004).
8. H. E. Andersen, R. J. McGaughey, S. E. Reutebuch, Estimating forest canopy fuel parameters using LIDAR data. Remote sensing of Environment, 94, 441-449(2005).
9 Steven C. Sherwood, Sandrine Bony, and Jean-Louis Dufresne, Spread in model climate sensitivity traced to atmospheric convective mixing, Nature, 55, 37-42, 2014.
10 Bony, S. & Dufresne, J. L. Marine boundary layer clouds at the heart of tropical cloud feedback uncertainties in climate models. Geophys. Res. Lett. 32, L20806, 2005.
11 Lin, B., P. Minnis, and A. Fan, Cloud liquid water amount variations with temperature observed during SHEBA experiment, J. Geophys. Res., 108 (D14), 4427, doi:10.1029/2002JD002851, 2003.
12 Lin, B., P. Minnis, T.F. Fan, Y. Hu, and W. Sun, Radiation characteristics of low and high clouds in different oceanic regions observed by CERES and MODIS, the International Journal of Remote Sensing, 31, 6473-6492, DOI: 10.1080/01431160903548005, 2010.
13 Lin, B., B.A. Wielicki, P. Minnis, L. Chambers, K.-M. Xu, Y. Hu, and A. Fan, The effect of environmental conditions on tropical deep convective systems observed from the TRMM satellite, J. Climate, 19, 5745-5761, 2006.

14. L. B. Lucy, An iterative technique for the rectication of observed images, The Astronomical Journal, 79, 745-754(1974).
15. J. Wu, J. A. N. van Aardt, G. P. Asner, A comparison of signal deconvolution algorithms based on small-footprint LiDAR waveform simulation, Geoscience and Remote Sensing, IEEE Transactions on, 49, 2402-2414(2011).
16. NRC, Earth Science and Applications from Space: National Imperatives for the Next Decade and Beyond, The National Academies Press, Washington, D.C., 2007
17. B. Lin, S. Ismail, F. W. Harrison, E. V. Browell, A. R. Nehrir, J. Dobler, B. Moore, T. Refaat, S. A. Kooi, "Modeling of intensity-modulated continuous-wave laser absorption spectrometer systems for atmospheric CO_2 column measurements," Appl. Opt., **50**(29), 7062-7077 (2013).
18. J. T. Dobler, F. W. Harrison, E. V. Browell, B. Lin, D. McGregor, S. Kooi, Y. Choi, and S. Ismail, "Atmospheric CO_2 column measurements with an airborne intensity-modulated continuous wave 1.57 μm fiber laser lidar," Appl. Opt., **52**(12), 2874-2892 (2013).
19. J. F. Campbell, B. Lin, A. R. Nehrir, F. W. Harrison, M. D. Obland, High Resolution CW Lidar Altimetry using Repeating Intensity Modulated Waveforms and Fourier Transform Reordering, Opt. Lett., 39, 6078 (2014).
20. J. F. Campbell, B. Lin, A. R. Nehrir, F. W. Harrison, M. D. Obland, Super-resolution technique for CW lidar using Fourier transform reordering and Richardson-Lucy deconvolution, **24**, 6981 (2014)
21. J. F. Campbell, Nonlinear swept frequency technique for CO_2 measurements using a CW laser system, Appl. Opt., 52, 3100 (2013).

22. D. S. C. Biggs and M. Andrews, Acceleration of Iterative Image Restoration Algorithms, Appl. Opt., 36, 1766(1997).
23. Obland, M., C. Antill, E. V. Browell, J. Campbell, S. Chen, C. Cleckner, M. Dijoseph, F. Harrison, S. Ismail, B. Lin, B. Meadows, C. Mills, A. Nehrir, A. Notari, N. Prasad, S. Kooi, N. Vitullo, J. Dobler, J. Bender, N. Blume, M. Braun, S. Horney, D. McGregor, M. Neal, M. Shure, T. Zaccheo, B. Moore, S. Crowell, P. Rayner, W. Welch, 2013 American Geophysical Union Fall Meeting, San Francisco, CA, December 9-13, 2013.
24. J. F. Campbell, B. Lin, A. R. Nehrir, F. W. Harrison, M. D. Obland, Binary Phase Shift Keying on Orthogonal Carriers for Multi-Channel CO_2 Absorption Measurements in the Presence of Thin Clouds, Opt. Exp., **22**, A1634 (2014).
25. J. F. Campbell, B. Lin, A. R. Nehrir, Advanced sine wave modulation of continuous wave laser system for atmospheric CO_2 differential absorption measurements, Appl. Opt., 53, pp. 816-829 (2014).
26. J. W. Hair, C. A. Hostetler, A. L. Cook, D. B. Harper, R. A. Ferrare, T.L. Mack, W. Welch, L. R. Izquierdo, and F. E. Hovis, Airborne High Spectral Resolution Lidar for profiling aerosol optical properties, Appl. Opt., 47, pp. 6734-6752